Monte Carlo calculations of X-ray scatter data for diagnostic radiology



1981 Phys. Med. Biol. 26 835

(http://iopscience.iop.org/0031-9155/26/5/003)

Phys. Med. Biol., 1981, Vol. 26. No. 5, 835–849. Printed in Great Britain

# Monte Carlo calculations of x-ray scatter data for diagnostic radiology

Willi Kalender,†

Medical Physics Division, Department of Radiology, University of Wisconsin, Madison, WI 53706, USA

Received 6 January 1981

**Abstract.** X-ray scatter data have been calculated by Mone Carlo methods for diagnostic radiology applications. The scatter intensities relative to the primary intensities are given for different detectors for various values of object thickness, field size, object-to-detector distance, and primary energy. The results are compared with those from previous investigations. The calculations made it possible to resolve contradictions in published measurements regarding the dependence of scatter intensities on primary X-ray energy and detector response.

## 1. Introduction

Scattered radiation constitutes a large, and often a major, contribution to the formation of the radiological image. The determination of its intensity relative to the intensity of the primary radiation has been the subject of numerous investigations, starting with Wilsey (1921). Both the qualitative dependence of the scatter fractions (defined below) on single parameters such as object thickness, field size, object-to-detector distance, primary energy, and their absolute values had to be determined. The data published so far are inconsistent; in particular, the dependence on the primary energy has not been fully determined.

We have chosen to investigate this problem through simulation, employing the Monte Carlo method: we first describe the method and present our results, and then discuss and compare them with previous investigations.

## 2. Method

The Monte Carlo (MC) method, implemented on a digital computer, is the method of choice in the investigation of diffusion problems of radiation in matter (Fano *et al* 1957). In addition, the theoretical approach not only ensures well defined and constant conditions, but also allows for investigations with monoenergetic sources and arbitrarily defined detectors. This has proved advantageous in resolving the discrepancies mentioned above.

A MC calculation of X-ray scatter is the repeated simulation of the passage of individual photons through a scattering medium: the computer program is a relatively short routine. As a direct analogue to a physical measurement, the MC calculation is terminated when a sufficient number of desired events, or hits, have been registered.

† Present address: Siemens AG, Medical Division, Henkestrasse 127, 8520 Erlangen, Fed. Rep. of Germany

0031-9155/81/050835+15 $1.50  

The result is not an expectation value, but a sample mean which underlies statistical fluctuations. The relative standard deviation is inversely proportional to the square root of the number of tries or photons started (Shreider 1966). A total of $10^6$ or more photon histories may be required to generate adequate statistics; both the repetitive character of MC calculations and the excessive computing times under certain conditions are evident. Our implementation of the MC method is described in detail elsewhere (Kalender 1979), where special attention is paid to measures that reduce computing times. An important step has been the use of tables of equiprobable scatter angles, first proposed by Hemmings (1967). This method substitutes the lengthy and less accurate generation of scatter angles by commonly used methods and has been extended to other random variables involved in our work.

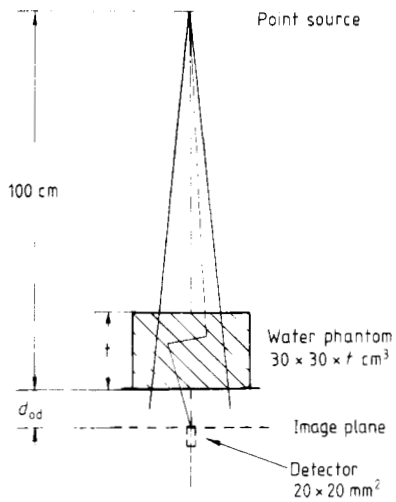


**Figure 1.** Geometry of the calculations. $t = 5$–$30$ cm. $d_{od} = 0$–$100$ cm. Field sizes up to 30 cm × 30 cm, or to a diameter of 36 cm.

The geometry underlying the calculations is shown in figure 1. A volume of water with a cross-section of 30 cm × 30 cm and thickness $t$ served as scatter medium; $t$ was varied from 5 to 30 cm. The source was assumed to be point-like and monoenergetic; the primary energy was varied from 30 to 150 keV. The distance from the source to the object exit plane was kept fixed at 100 cm. The field size (FS), measured in the exit plane, covered the range up to 30 cm × 30 cm or a diameter of 36 cm for circular fields. The object-to-detector distance $d_{od}$ was varied from 0 to 100 cm.

For each photon passing through the object exit plane we calculated the absorbed energy, $\Delta E$, for each assumed detector position, in case it was hit, and for several detector materials and thicknesses, where

$$\Delta E = E_s\{1 - \exp[(-\mu_{en}(E_s)/\rho)t_{det}]\}.$$

$E_s$ denotes the energy of the scattered photon, $\mu_{en}/\rho$ is the mass energy absorption coefficient and $t_{det}$ the thickness in g cm$^{-2}$ for the detector involved. $\mu_{en}/\rho$ includes the photoelectric and incoherent scattering absorption coefficients, $\sigma_a$(photo) and $\sigma_a$(incoh); the values were taken from the tables of Storm and Israel (1970).

The relative standard deviation in the results presented below was determined to be about 2%.

## 3. Definitions

We will specify our results in terms of scatter fractions, $F$. We define the scatter fraction for numbers of quanta as

$$F_N = N_s/(N_p + N_s) \tag{1}$$

where $N_s$ is the number of scattered quanta and $N_p$ is the number of primary quanta. $N_t = N_p + N_s$ is the total number of quanta. The scatter fraction for intensities is defined as

$$F_I = I_s/(I_p + I_s) \tag{2}$$

with the subscripts defined above.

The numerical values for $F_N$ have to be higher than those for $F_I$ for identical measurements or calculations because the energy $E_s$ of the scattered quanta lies below the primary energy $E_p$, giving

$$F_N = N_s/(N_p + N_s) > (N_s E_s/(N_p E_p + N_s E_s) = F_I. \tag{3}$$

The quantitiy $F_I$ is used only when the detector has an efficiency of one, i.e. when both primary and scattered radiation are fully absorbed irrespective of the initial energy. The condition can most easily be met in a simulation, but also occurs with scintillation detectors of appropriate thickness. Whenever a 'thin' detector (i.e. a detector with an efficiency essentially below unity) is employed we will indicate this by primed symbols $I'_s$, $F'_I$, etc., specifying the detector in parantheses, e.g. $F'_I$ (80 mg cm$^{-2}$ $CaWO_4$). x-ray intensifying screens and image intensifier input screens, the standard detectors in transmission radiography, are such thin detectors for the commonly used spectra.

## 4. Results and discussion

### *4.1. Scatter fractions*

*4.1.1. The dependence on detector thickness and material.* When primary and scattered intensities $I_p$ and $I_s$ are incident on a detector of thickness $t_{det}$,

$$I'_p = I_p\{1 - \exp[(\mu_{en}(E_p)/\rho)t_{det}]\} \tag{4}$$

and

$$I'_s \simeq I_s[1 - \exp[(-\mu_{en}(\bar{E}_s)/\rho)(t_{det}/\cos\bar{\beta})]] \tag{5}$$

will be recorded, where $\bar{E}_s$ and $\bar{\beta}$ are the mean energy and the mean angle of incidence of the scattered photons, respectively. As a higher fraction of $I_s$ will be absorbed than of $I_p$ (we disregard detector K-absorption edges at this point) $F'_I$ will be larger than $F_I$. The numerical difference is determined by the detector thickness.

The dependence on detector thickness is shown in figure 2 for a $CaWO_4$ screen at 60 keV primary energy, for 10 cm object thickness and two field sizes. The $F'_I$ values decrease from an upper limit for $t \to 0$ towards a lower limit for $t \to \infty$. The value of the lower limit corresponds to $F_I$, the value recorded with a detector of efficiency one, hereafter referred to as Eff 1.

These results can easily be understood. When $t_{det}$ is increased to high values, the exponentials in equations (4) and (5) approach zero and $F'_I$ approaches $F_I$. When $t_{det}$ approaches zero, we obtain

$$\lim_{t_{det}\to 0} F'_I = (a\mu_{en}(\bar{E}_s)/\cos\bar{\beta})/(\mu_{en}(E_p) + a\mu_{en}(\bar{E}_s)/\cos\bar{\beta}) \tag{6}$$

where $a = I_s/I_p$.

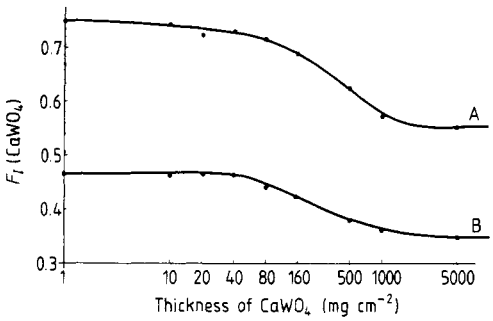


**Figure 2.** Scatter fractions as a function of detector thickness. $E = 60$ keV, $t = 10$ cm, $d_{od} = 4$ cm. Curve A, FS = 30 cm × 30 cm. Curve B, FS = 10 cm × 10 cm.

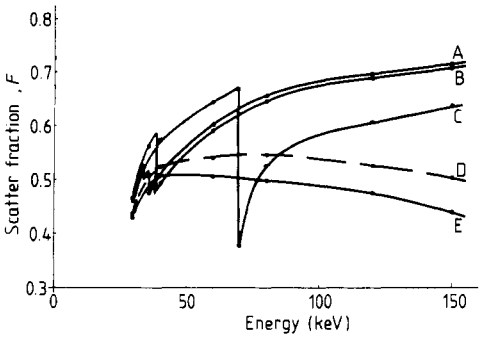


**Figure 3.** Scatter fractions for different detectors. $t = 10$ cm. FS = 20 cm × 20 cm. $d_{od} = 4$ cm. Detector particulars for the curves are: A, $F_I'$ (60 mg cm$^{-2}$ CsI); B, $F_I'$ (90 mg cm$^{-2}$ LaOBr); C, $F_I'$ (80 mg cm$^{-2}$ $CaWO_4$); D, $F_N$; E, $F_I$.

The curves in figure 2 will be shifted slightly left for energies below 60 keV and right for energies above 60 keV, because the limits will be approached at smaller and greater detector thicknesses for increasing and decreasing $\mu_{en}(E)$ values, respectively. The scatter fractions recorded for an object thickness of 10 cm and a field size of 20 cm × 20 cm are shown in figure 3 for different detectors as a function of energy. We chose CsI of 60 mg cm$^{-2}$ thickness representing an image intensifier input screen, an 80 mg cm$^{-2}$ $CaWO_4$ screen as recommended by the ICRU (1962) for grid evaluations, and LaOBr of 90 mg cm$^{-2}$ thickness representing a commercially available rare earth screen (Siemens Titan U intensifying screen). The scatter fractions $F_I$ and $F_N$ for an Eff 1 detector are also shown. The differences between the detector materials are essentially given by the different positions of the K-absorption edge. For a monoenergetic source with energy just above the K-edge the major portion of scatter will have energies below the K-edge and a correspondingly reduced probability for absorption. For conventional broad spectra this effect remains undetected.

The heights of the curves for the three thin detectors relative to each other are determined by the factor $\mu_{en}/t_{det}$. For example, above the K-edges $\mu_{en}/t_{det}$ is smaller for the CsI-screen than for the LaOBr screen; thus the CsI screen represents the 'thinner' detector with higher relative scatter sensitivity.

*4.1.2. Dependence on primary energy.* We first discuss the dependence of $F_I$ on energy and then the scatter fractions measured by thin detectors.

The scatter fractions $F_I$ and $F_N$ graphed in figure 4 show essentially the same energy dependence. The difference between $F_I$ and $F_N$ values increases with energy and with the size of the irradiated volume as multiple scatter becomes predominant and the average energy of the scattered quanta lie further below the primary energy (see section 4.3). In the following discussion we concern ourselves with the scatter fraction of intensities, $F_I$, only. Single and multiple scatter, which were input separately into the calculations, exhibit approximately the same energy dependence, and we need not treat them separately.

Two factors govern the energy dependence:

(i) The scatter intensity originating from a volume element of thickness $\Delta$ in the scattering medium is proportional to $1\text{-}\exp(-\mu_s\Delta)$ or roughly proportional to $\mu_s$, where

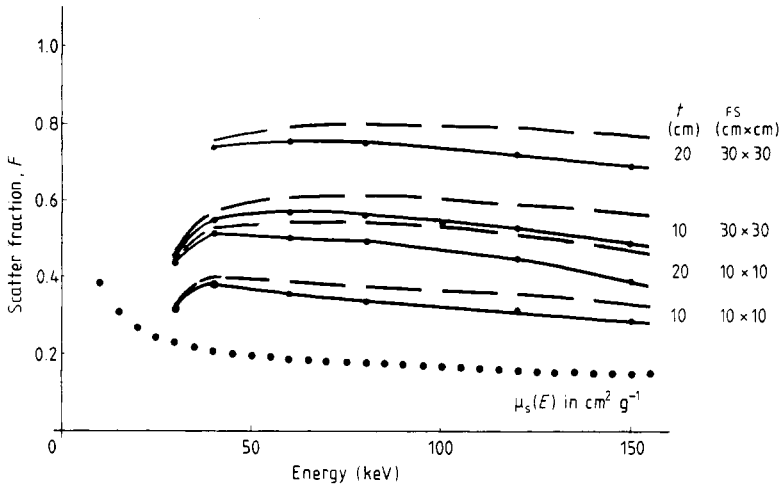


**Figure 4.** Scatter fractions as a function of energy. $d_{od} = 4$ cm. No grid. Solid line, $F_I = I_s/I_t$. Dashed line, $F_N = N_s/N_t$.

$\mu_s$ is the sum of the coherent and incoherent scatter coefficients. $\mu_s$ decreases with increasing energy and has high values at low energies where coherent scatter is appreciable (see dotted line in figure 4).

(ii) On the path from the point of origin to the point of exit from the object, the attenuation of scattered radiation is larger than that of primary radiation, primarily because of the increased path length and to a much lesser degree because of the lower energy.

Combining these two factors explains the energy dependence shown in figure 4. At high energies where the object approximates a pure scatterer, $\mu_s(E)$ dominates; the scatter fractions fall off slowly with energy. Towards low energies absorption due to photoelectric processes, and thereby the second factor, becomes dominant; the scatter fractions fall off fast towards low energies. (For the same reason calculation times become prohibitively long; no calculations below 30 keV were carried out.) For large irradiated volumes, with a high proportion of multiple scatter and correspondingly longer path lengths, the second factor remains influential at higher energies than is the case for small irradiated volumes, shifting the maxima in figure 4 correspondingly. The energy dependence shown in figure 4 holds for Eff 1 detectors.

Scatter fractions recorded with thin x-ray detectors will increase with energy as shown in figure 3. The difference between $F_I$ and $F'_I$ values is small at low energies, where the efficiency of the chosen detectors approaches one, but increases with energy where they become thin detectors. For the same reason the K-edge discontinuity in $F'_I$ is smaller for CsI and LaOBr then for $CaWO_4$ for the chosen detector thicknesses.

The difference between $F_I$ and $F'_I$ increases with energy (see figure 3), and is approximately described by

$$d_F = \frac{ay}{(1+a)y} - \frac{a}{1+a}$$

where

$$y = (\mu_{en}(\bar{E}_s)/\cos\bar{\beta})/\mu_{en}(E_p)$$

$$a = I_s/I_p$$

and $F_I'$ is taken from equation (6). $1/\cos\bar{\beta}$ increases only slightly with energy for our conditions (see section 4.3). The increase in $d_F$ with energy is caused by an increase in the ratio of $\mu_{en}(\bar{E}_s)/\mu_{en}(E_p)$ due to the growing difference between $\bar{E}_s$ and $E_p$, the mean energy of scattered radiation and of primary radiation, respectively. $\bar{E}_s$-values are given in table 1 for a small and a large irradiated volume.

**Table 1.** Mean energy of scattered radiation and mass energy absorption coefficients for CsI. s, m and t stand for single, multiple and total scatter. $d_{od} = 4$ cm, $t_{det}(CsI) = 60$ mg cm$^{-2}$.

| Primary energy (keV) | $(\mu/\rho)_{en}(E_p)$ (cm$^2$ g$^{-1}$) | FS = 10 cm × 10 cm, $t$ = 10 cm | | | | FS = 30 cm × 30 cm, $t$ = 20 cm | | | |
|---|---|---|---|---|---|---|---|---|---|
| | | $\bar{E}_s$ (keV) | | | $\frac{\mu_{en}(\bar{E}_s)_t}{\mu_{en}(E_p)}$ | $\bar{E}_s$ (keV) | | | $\frac{\mu_{en}(\bar{E}_s)_t}{\mu_{en}(E_p)}$ |
| | | s | m | t | | s | m | t | |
| 30 | 8.05 | 29.8 | 28.0 | 29.0 | 1.12 | — | — | — | — |
| 40 | 22.35 | 39.5 | 35.6 | 37.7 | 1.16 | 39.5 | 35.5 | 36.6 | 1.26 |
| 60 | 7.52 | 58.7 | 48.8 | 53.6 | 1.36 | 58.8 | 47.2 | 49.7 | 1.67 |
| 80 | 3.39 | 77.6 | 61.5 | 69.2 | 1.50 | 77.6 | 57.3 | 61.7 | 2.06 |
| 120 | 1.10 | 114.8 | 82.7 | 98.7 | 1.71 | 114.5 | 74.3 | 82.7 | 2.80 |
| 150 | 0.587 | 141.8 | 96.2 | 120.7 | 1.84 | 141.1 | 85.2 | 98.6 | 3.20 |

*4.1.3. Dependence on field size and shape.* Scatter fractions increase with field size FS, most sharply at the smallest fields (see figure 5). The rate of increase depends slightly on the primary energy as shown in figure 6. $F_I$ increases very little when going to larger fields at low energies as absorption is too strong.

The dependence on field shape was only verified for fields of about 200 cm$^2$ at an object thickness of 10 cm and an object-to-detector distance of 4 cm at 60 keV primary energy. For a circular field of 16 cm diameter (201 cm$^2$) and a square field of 14 cm × 14 cm (196 cm$^2$) scatter fraction values of 44.5% and 44.6% respectively were obtained, which means no significant difference. For rectangular fields of 10 cm × 20 cm and 7 cm × 30 cm, $F_I$ decreased to 39.7% and 36.7% respectively. This decrease results from the increased distance between the detector and the scattering volume elements.

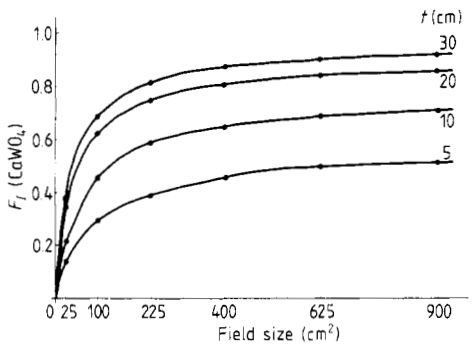


**Figure 5.** Scatter fractions as a function of field size and object thickness. $E = 60$ kev. $d_{od} = 4$ cm. Detector: 80 mg cm$^{-2}$ $CaWO_4$.

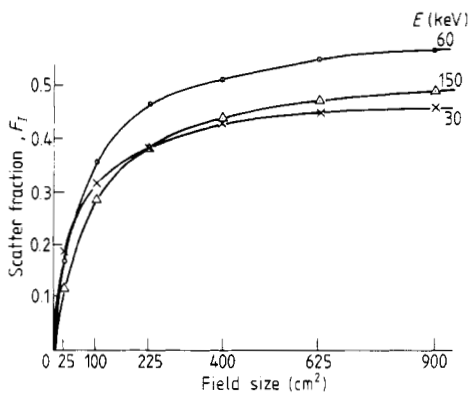


**Figure 6.** Scatter fractions as a function of field size for different energies, $E$. $t = 10$ cm. $d_{od} = 4$ cm.

*4.1.4. Dependence on object thickness.* Scatter fraction values $F_I'$ ($CaWO_4$) for several object thicknesses were shown in figure 5. Scatter fractions initially increase rapidly with thickness and more slowly at higher values. This is seen in the definition $F_I = I_s/(I_p + I_s)$. The ratio $I_s/I_p$, which is known as the build-up factor $B$, does not approach a maximum value. It keeps increasing almost linearly.

Computing times increase considerably for greater object thicknesses and for low energies. For $t = 30$ cm, the calculations were carried out at 60 keV only. For $t =$ 20 cm, the 30 keV calculations were limited to a 10 cm × 10 cm field.

*4.1.5. Dependence on object-to-detector distance.* Scatter fraction values decrease rapidly as the object-to-detector distance $d_{od}$ is increased. The rate of decrease clearly depends on the field size, but only little on the object thickness (see figure 7).

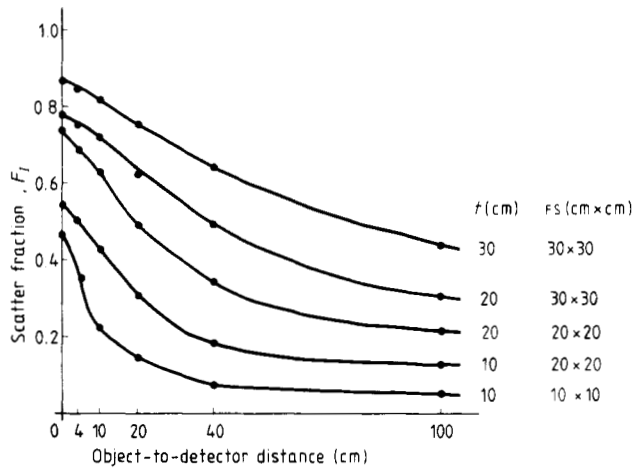


**Figure 7.** Scatter fractions as a function of object-to-detector distance. $E = 60$ keV.

Most of the scatter reaches the detector from the last few object layers (see section 4.3). Therefore we approach a point source for very small fields with an intensity fall-off corresponding to the $1/r^2$ law, whereas for large fields and small object-to-detector distances we approach a plane source with no distance dependence for distances small compared to the source dimensions. Neither model strictly applies; the second one especially is limited. However, they help to understand qualitatively the field size dependence factor in the intensity decrease with object-to-detector distance.

The air gap technique employs the fact that the scatter intensity decreases faster than the primary intensity behind the object because of the shorter distance to the source. The false assumption that the scatter intensity falls with $1/r^2$ (Trout *et al* 1975) overestimates the scatter supression by increasing the object-to-detector distance.

*4.1.6. Numerical values.* Numerical sample values from our calculations are assembled in table 2 for easier reference. Results are given for different field sizes, detectors and energies for 5, 10, 20 and 30 cm water thickness respectively. The table refers to an object-to-detector distance of 4 cm. The agreement with numerical values from other studies will be discussed in the next section.

**Table 2.** Scatter fraction results in %.

| Object thickness (cm) | 5 | 10 | | | | | | 20 | | | | | | 30 |
|---|---|---|---|---|---|---|---|---|---|---|---|---|---|---|
| Energy (keV) | 60 | 30 | 40 | 60 | 80 | 120 | 150 | 30 | 40 | 60 | 80 | 120 | 150 | 60 |
| Field size (cm) Detectors | | | | | | | | | | | | | | |
| 10×10 $F_I'$ ($CaWO_4$) | 29.5 | 33.5 | 42.7 | 45.5 | 34.8 | 40.1 | 42.5 | 47.4 | 56.0 | 62.3 | 50.0 | 55.9 | 57.4 | 69.2 |
| $F_I'$ (LaOBr) | 26.9 | 33.7 | 37.5 | 41.3 | 44.5 | 47.7 | 49.0 | 47.7 | 49.5 | 57.1 | 61.7 | 66.8 | 66.9 | 69.0 |
| $F_I'$ (CsI) | 27.4 | 34.8 | 38.6 | 42.2 | 45.4 | 48.4 | 49.6 | 48.9 | 50.6 | 58.1 | 62.6 | 67.7 | 67.9 | 65.0 |
| $F_I$ | 22.7 | 31.8 | 38.6 | 35.8 | 33.5 | 31.0 | 28.6 | 45.6 | 51.2 | 50.2 | 49.0 | 44.5 | 39.2 | 57.0 |
| $F_N$ | 24.1 | 32.4 | 39.8 | 38.2 | 37.0 | 34.9 | 32.9 | 46.3 | 52.7 | 53.6 | 53.5 | 50.9 | 46.3 | 60.6 |
| 20×20 $F_I'$ ($CaWO_4$) | 45.7 | 46.1 | 57.3 | 64.8 | 52.7 | 60.7 | 63.7 | — | 72.7 | 80.5 | 70.2 | 77.0 | 79.6 | 87.9 |
| $F_I'$ (LaOBr) | 40.8 | 46.5 | 49.4 | 59.3 | 64.6 | 68.8 | 70.8 | — | 65.4 | 76.0 | 80.8 | 84.8 | 85.9 | 84.0 |
| $F_I'$ (CsI) | 41.7 | 46.1 | 51.5 | 60.4 | 65.5 | 69.4 | 71.5 | — | 67.1 | 76.9 | 81.6 | 85.4 | 86.5 | 84.8 |
| $F_I$ | 32.8 | 43.0 | 50.8 | 51.2 | 49.8 | 46.9 | 43.8 | — | 67.2 | 69.0 | 68.7 | 65.0 | 61.5 | 78.5 |
| $F_N$ | 35.2 | 43.9 | 52.4 | 54.5 | 54.6 | 52.6 | 50.4 | — | 68.9 | 72.4 | 73.5 | 71.8 | 69.5 | 81.3 |
| 30×30 $F_I'$ ($CaWO_4$) | 51.5 | 49.1 | 62.1 | 71.1 | 59.8 | 67.6 | 70.7 | — | 78.6 | 86.0 | 77.0 | 83.4 | 85.3 | 92.1 |
| $F_I'$ (LaOBr) | 45.7 | 49.5 | 53.3 | 65.6 | 71.3 | 74.8 | 77.4 | — | 70.4 | 81.8 | 86.1 | 89.4 | 90.2 | 89.5 |
| $F_I'$ (CsI) | 46.8 | 52.1 | 55.5 | 66.7 | 72.3 | 75.5 | 78.1 | — | 73.2 | 82.8 | 86.7 | 89.9 | 90.7 | 90.1 |
| $F_I$ | 36.2 | 45.6 | 54.6 | 56.7 | 55.7 | 52.5 | 49.0 | — | 73.0 | 75.3 | 75.1 | 72.2 | 68.7 | 85.1 |
| $F_N$ | 38.9 | 46.6 | 56.4 | 60.1 | 60.7 | 58.5 | 56.6 | — | 74.7 | 78.6 | 79.5 | 78.6 | 76.4 | 87.4 |

$CaWO_4$: 80 mg $cm^{-2}$. LaOBr: 90 mg $cm^{-2}$. CsI: 60 mg $cm^{-2}$. $d_{od}$ = 4 cm.

### *4.2. The distribution of scattered radiation in the image plane*

The distribution of the intensity of scattered radiation has been registered for $20 \times 20$ pixels of 1 $cm^2$ size in the first quadrant at 4 cm object-to-detector distance and along the field axes and the field diagonal for 10, 20, 40 and 100 cm object-to-detector distance. Statistical fluctuations are large at higher object-to-detector distances.

The scatter intensity at any point in the image plane is the sum of the superimposed intensities originating from all volume elements of the object. A fall-off in scatter intensity has to occur for points away from the central ray because the average distance to the volume elements and the intervening object thickness increase. The fall-off will be slower for greater object-to-detector distances because the change in the above distances is smaller.

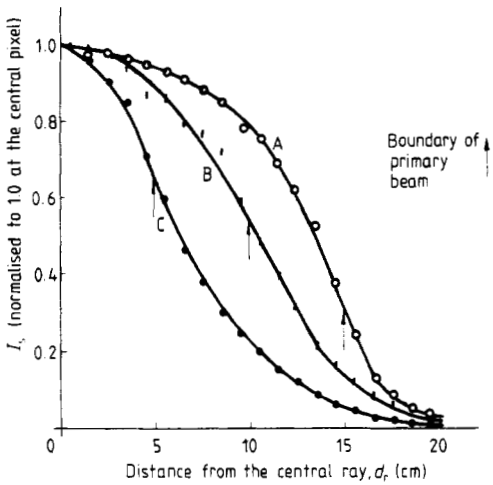


**Figure 8.** Distribution of scatter in the image plane as a function of distance from the central ray, $d_r$. $E = 60$ keV. $t = 10$ cm. $d_{od} = 4$ cm. Field sizes (cm × cm): A, 30 × 30; B, 20 × 20; C, 10 × 10.

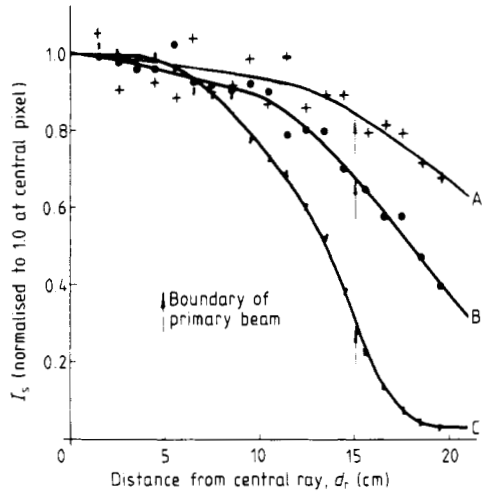


**Figure 9.** Distribution of scatter in the image plane as a function of $d_r$. $E = 60$ keV. $t = 20$ cm. FS = 30 cm × 30 cm. Values of $d_{od}$ for the curves: A, 40 cm; B, 20 cm; C, 4 cm.

These qualitative considerations were confirmed by the calculations. The intensity fall-off is plotted in figure 8 for several field sizes at 4 cm object-to-detector distances and figure 9 for a 30 cm × 30 cm field at different object-to-detector distances, with the intensity values normalised to 1.0 at the central pixel. The fall-off is generally very strong, with a reduction to 65%, 53% and 32% at the boundary of the primary field for field sizes of $10 \times 10$, $20 \times 20$ and $30 \times 30$ $cm^2$ respectively. There was no significant dependence on object thickness, as illustrated by the curves for 4 cm object–detector distance and $30 \times 30$ $cm^2$ field size in figures 8 and 9.

### *4.3. Additional results on scattered radiation*

As a byproduct of the above calculations further information on scattered radiation has become available.

*4.3.1. The angular and energy distribution.* The mean energy, $\bar{E}_s$, and the mean cosine of the angle of incidence at the detector, $\overline{\cos \beta}$, for single, multiple and total scatter have

**Table 3.** Mean angle of incidence for scattered radiation (s, m, t—single, multiple, total scatter), $d_{od} = 4$ cm, 60 mg cm$^{-2}$ CsI detector, mean angle of incidence $\bar{\beta} = \cos^{-1}(\overline{\cos\beta})$

| Primary energy (keV) | FS = 10 cm × 10 cm, $t$ = 10 cm | | | FS = 30 cm × 30 cm, $t$ = 20 cm | | |
|---|---|---|---|---|---|---|
| | s | m | t | s | m | t |
| 30 | 27.8 | 36.7 | 32.1 | — | — | — |
| 40 | 30.0 | 36.2 | 33.1 | 28.1 | 38.1 | 34.9 |
| 60 | 32.3 | 38.1 | 35.4 | 32.3 | 41.9 | 40.0 |
| 80 | 33.2 | 37.3 | 35.4 | 34.0 | 42.1 | 40.4 |
| 120 | 32.9 | 38.5 | 35.8 | 34.9 | 43.4 | 41.7 |
| 150 | 33.4 | 38.7 | 36.0 | 36.0 | 43.8 | 42.0 |

been determined in each calculation. Mean energy values have been presented in table 1; mean angles of incidence are given in table 3 for the same parameters, where $\bar{\beta}$ represents $\bar{\beta} = \cos^{-1}(\overline{\cos\beta})$.

The mean energy of single scatter falls little below the primary energy. The energy degradation of multiple scatter is considerable, however, and is most notable for large irradiated volumes where the average number of interactions increases. The mean energy of the total scatter reflects the percentage of single and multiple scatter in the total. The mean angle of incidence changes little with energy; it increases slightly because oblique (i.e. longer) paths are only probable at higher energies. Single scatter is more forward oriented than multiple scatter—the average angle of incidence is smaller.

*4.3.2. The source distribution and multiple scatter contributions.* The scattered photons have been recorded by layer of origin. The layer of origin is here defined as the object slice of 2 cm thickness perpendicular to the central ray where the photon was scattered before hitting the detector. The layer $i$ extends from $t' = 2(i-1)$ to $t' = 2i$ starting at the entrance point. Table 4 gives the contributions from each 2 cm layer as a percentage of the total for several volumes. Our results justify estimates appearing in the literature

**Table 4.** The scatter source distribution, $I_s(i)/I_s$, per 2 cm layer $i$. $E = 60$ keV, $d_{od} = 4$ cm.

| FS (cm × cm) | 10 × 10 | 30 × 30 | 10 × 10 | 30 × 30 |
|---|---|---|---|---|
| $t$ (cm) | 10 | 10 | 20 | 20 |
| $i = 1$ | 8.4 | 9.3 | 2.4 | 2.0 |
| 2 | 13.6 | 13.2 | 3.4 | 3.4 |
| 3 | 17.3 | 16.5 | 2.9 | 3.3 |
| 4 | 23.5 | 23.8 | 3.0 | 3.7 |
| 5 | 37.2 | 37.1 | 5.7 | 6.5 |
| 6 | | | 6.8 | 7.6 |
| 7 | | | 11.2 | 11.3 |
| 8 | | | 14.3 | 14.4 |
| 9 | | | 20.1 | 20.1 |
| 10 | | | 30.2 | 27.8 |

Layer $i$ ranges from $2(i-1)$ to $2i$ cm along the central ray.

(e.g. Reiss 1959) that the major fraction of scatter intensity results from the last few object layers. There was no significant energy dependence.

The ratio of multiple to single scatter intensity, $I_s^m/I_s^s$, is shown in figure 10 as a function of field size for several object thicknesses. Single scatter dominates for small irradiated volumes, multiple scatter in large ones. $I_s^m/I_s^s$ was only evaluated up to a field size of 15 cm × 15 cm for $t = 30$ cm.

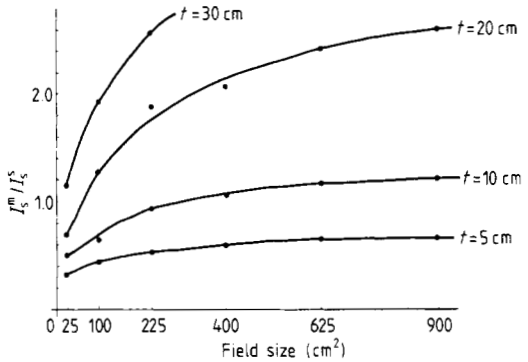


**Figure 10.** Ratio of multiple to single scatter intensity. $E = 60$ keV. $d_{od} = 4$ cm. No grid. Object is 30 cm × 30 cm × $t$ cm of water.

*4.3.3. The dependence of scatter fractions on the object cross-section.* Generally, a water block of 30 cm × 30 cm cross-section was assumed in the calculations. In a test calculation we changed these values to determine the influence of the object dimensions. For smaller cross-sections the $F_I$ values decrease because less multiple scatter results. At large dimensions the scatter fractions increase (see table 5); however, the computing times increase even more strongly because photons are followed a considerable distance from the central ray and do not result in detector hits.

**Table 5.** Scatter fractions for different object sizes. $E = 60$ keV, $d_{od} = 4$ cm, $t = 10$ cm, FS = 10 cm × 10 cm.

| Cross section of water block (cm × cm) | $F_I$ (%) |
|---|---|
| 10 × 10 | 29.1 |
| 10 × 30 | 30.5 |
| 30 × 30 | 31.1 |
| 100 × 30 | 33.5 |

The 30 cm × 30 cm cross-section appears reasonable; it was kept for all calculations and corresponds to the dimensions recommended by the ICRU (1962) for the evaluation of grids. For special calculations, such as scatter fractions in pediatric radiology or mammography, other object dimensions have to be chosen.

## 5. Comparison with previous investigations

### 5.1. General review

There is qualitative agreement between measurements and our calculations for the trends in the dependence of the scatter fractions on object thickness, field size and object-to-detector distance. $F$ will increase with field size and object thickness and decrease with object-to-detector distance; the interrelation with other parameters has been discussed.

The distribution of the scatter intensity along the field axes was measured by Zieler (1964) for two field sizes. His results are in very good agreement with our values. Further consideration of the subject by Nemet *et al* (1953) and Führ (1975) was merely qualitative.

A comparison with numerical scatter fraction values is difficult in that the experimental results of different authors are not consistent. No safe conclusions as to the correctness of our calculations can therefore be drawn from the measurements.

**Table 6.** Comparison of scatter fraction results.
(a) Measurements with film–screen combinations.

| Reference | Tube voltage | $t = 10$ cm $\phi = 10$ cm | 20 cm |
|---|---|---|---|
| Wilsey (1921)[1,6] | —[7] | 41 | 48 |
| Nemet *et al* (1954)[2] | 125 $kV_p$ | 29 | 72 |
| Gajewski (1954)[1] | 125 $kV_p$ | 35 | 83 |
| Goodwin *et al* (1970)[1] | 100 $kV_p$ | — | 80[3] |
| Reiss and Steinle (1973)[2] | 100 $kV_p$ | 44 | 80 |
| Führ (1975)[1] | 80 $kV_p$ | 61 | 84 |
| Stargardt and Angerstein (1975)[1,4] | 105 $kV_p$ | 57 | 81 |
| Our data[2,5] | 60 keV | 42 | 79 |

[1] $d_{od}$ not specified, detector 'behind' phantom.
[2] $d_{od} = 4.0$ cm.
[3] For field size 300 $cm^2$.
[4] For a field of 10 cm × 10 cm.
[5] MC calculation for a $CaWO_4$ screen of 80 g $cm^{-2}$.
[6] Measured with plain film.
[7] Spark gap of 5 in.

(b) Measurements with detectors having an efficiency of one.

| Field diameter (cm) | 10 | | 20 | |
|---|---|---|---|---|
| Object thickness (cm) | 10 | | 20 | |
| | $F_N$ | $F_I$ | $F_N$ | $F_I$ |
| Reiss und Steinle (1973)[1] | 49.2 | 46.4 | 74.1 | 70.6 |
| Dick *et al* (1978)[2] | 56.0 | — | 83.0 | — |
| Our data[3] | 47.6 | 44.9 | 75.5 | 72.4 |

[1] MC calculation, $d_{od} = 0.0$ cm, 100 $kV_p$, 2 mm Al.
[2] Measurement with NaI crystal, $d_{od} = 0.3$ cm, 69 keV, $t = 21$ cm in the second measurement.
[3] MC calculation, $d_{od} = 0.0$ cm, 60 keV.

Numerical values of scatter fractions from the best known previous studies are summarized in tables 6a and 6b. The measured values for film–screen combinations vary widely for the small irradiated volume. Nemet *et al* (1953) reported low values and no explanation can be given. Führ (1975) and Stargardt and Angerstein (1975) quote higher results; again, the description of the experiments does not allow conclusions about the correctness. Führ does not give a description of his apparatus.

For the larger volume, the results are in good agreement. Wilsey's low value can be partially understood from figure 6; at the low tube voltage he was using the scatter fraction no longer increases significantly with field size (the exact tube voltage cannot be determined from the description).

For Eff 1 detectors (see table 6*b*) results were available from another MC study (Reiss and Steinle 1973) and from measurements with monoenergetic radiation (Dick *et al* 1978). The agreement between the MC calculations is good. The data from Reiss and Steinle were obtained by both measurements and calculations; their set-up is well defined and conformed to the ICRU (1962) recommendations. We have no explanation for the numerical difference between the calculations and the measurements of Dick *et al* (1978); the difference in results on the energy dependence is discussed below.

### *5.2. The dependence on primary energy*

An apparent discrepancy in the measured data concerns the energy dependence. Dick *et al* (1978) stated: 'Previous data have indicated that $F$ increases (Goodwin *et al* 1970), decreases (Halmshaw 1966, Motz and Dick 1975) or has negligible variation (Reiss and Steinle 1973) as the x-ray energy increases from 30 to 70 keV.'

The dependence on the initial energy of the radiation or the incident spectrum did not appear contradictory for a long time. All workers who measured scatter fractions with broad x-ray spectra and standard x-ray screens, mostly $CaWO_4$-screens, found a slow increase with increasing tube voltages and a leveling-off at higher voltages. Albers-Schönberg (1902) stated an increase in 'fogging' as he increased the tube voltage. The same findings were reported by Wilsey (1921), Nemet *et al* (1953), Gajewski (1954), Spiegler (1957), Goodwin *et al* (1970), Reiss and Steinle (1973), Führ (1975), Friedrich (1975) and Stargardt and Angerstein (1975). This is in accordance with our findings for monoenergetic sources which can be applied to any spectrum by combining the results. The scatter fraction for thin detectors increases with energy. When using broad x-ray spectra this increase is not immediately apparent as the mean energy rises only slowly. Above 80 $kV_p$, the tungsten K-edge can be held responsible for suppressing further increase in the scatter fraction recorded with $CaWO_4$ screen (see figure 3).

In apparent contradiction, Motz and Dick (1975) reported that the scatter fraction decreased with increasing primary energy. They used monoenergetic sources from 18 to 660 keV and a thick NaI crystal. In a further study (Dick *et al* 1978), they found no energy dependence. Halmshaw (1966) stated that the scatter fractions measured with thin lead foils used as intensifying screens in industrial radiography decreased with energy for energies from 200 kV to 15 MeV. The stated conditions are not covered by this study. The data by Motz and Dick (1975) and by Dick *et al* (1978) were both obtained with a NaI-crystal, efficiency = 1. Their first measurements, carried out at seven energy values, are in accordance with our results for Eff 1 detectors in that the scatter fraction $F_I$ decreases for higher energies. The low energy results have since been revised in their second publication; they were too high. Their recent measurement

was carried out for two energy values only, which gave equal scatter fractions; they concluded that there is no energy dependence. Additional measurements appear necessary, and should then be compared with the curves in figure 3. (Note that Dick *et al* (1978) compared their $F_N$ measurements to $F_I'$ values from the literature. The definitions given in section 3 have to be kept in mind.)

### *5.3. Conclusions*

The theoretical approach to problems of evaluating parameters of scattered radiation is advantageous. The set-up is well defined and no unwanted or unknown side-effects occur. The variability in the choice of parameters is unlimited as long as computing times are acceptable. Arbitrary x-ray sources and idealised detectors can be postulated.

Taking into account the difficulties in interpreting the experimental results, our calculations compare well with the measurements. Further confirmation and confidence were gained in observing that the method is very sensitive to changes of all parameters and that all observed trends conform to physical considerations. The apparent discrepancies in the measured data could probably be resolved if the measurement conditions were described precisely. The discrepancy in the results on the energy dependence, reported by Dick *et al*, has been resolved by pointing out the role of the detector—the dependence looks different for Eff 1 detectors and for thin detectors as was shown in section 4.1.2. It is absolutely necessary to specify all experimental parameters.


## Résumé

Calcul de la valeur du rayonnement diffusé $X$ par la méthode de Monte Carlo pour le diagnostic radiologique.

Les valeurs du rayonnement diffusé $X$ ont été calculées par la méthode de Monte Carlo pour des applications au diagnostic radiologique. Les intensités du rayonnement diffusé, relatives aux intensités initiales sont données pour différents détecteurs, pour des objets d'épaisseur variable et l'énergie initiale. Nous avons comparé les résultats obtenus à ceux d'études précedentes. Les calculs ont permis de résoudre les contradictions dans les mesures déjà publiées à propos de la dépendance des intensités du rayonnement diffusé sur l'énergies initiale des rayons $X$ et la résponse du détecteur.

## Zusammenfassung

Monte-Carlo-Berechnungen von Röntgenstrahlstreudaten in der Röntgendiagnostik.

Für röntgendiagnostische Anwendungen wurden Röntgenstrahlstreudaten mit Hilfe der Monte-Carlo-Methode berechnet. Für verschiedene Objecktdicken, Feldgrößen, Objekt-Detektor-Entfernungen und verschiedene Anfangsenergie werden Streuintensitäten relativ zur Angangsintensität für unterschiedliche Detektoren angegeben. Die Ergebnisse werden mit den Resultaten früherer Untersuchungen verglichen. Indem man die Abhängigkeit der Streuintensitäten von der Anfangsenergie der Röntgenstrahlen und der Detektor-Rückantwort berücksichtigt, kann man mit den Berechnungen Widersprüche in publizierten Messungen lösen.


## References


Albers-Schönberg H E 1901 *Fortschr. Geb. Roentgenstr.* **5** 301–8

Dick C E, Soares C G and Motz J W 1978 *Phys. Med. Biol.* **23** 1076–85

Fano U, Spencer L K and Berger M J 1959 *Encyclopedia of Physics* Vol XXXVIII 12 ed S Flügge (Berlin: Springer-Verlag) pp 660–817

Friedrich M 1975 *Fortschr. Geb. Roentgenstr.* **123** 556–66
Führ K P 1975 *Radiol. Diagn.* **3** 457–64
Gajewski H 1954 *Forstschr. Geb. Roentgenstr.* **80** 643–9
Goodwin P N, Quimby E H and Morgan R H 1970 *Physical Foundations of Radiology* 4th edn (New York: Harper and Row)
Halmshaw R 1966 *Physics of Industrial Radiography* (New York: Elsevier) p 142
Hemmings P J 1967 *The GEM Code* UKAEA Report AHSB(S) R105 1959
ICRU 1962 *Methods of Evaluating Radiological Equipment and Materials* Report 10f (NBS Handbook 89) (ICRU Publications, PO Box 30165, Washington, DC 20014, USA)
Kalender W A 1979 *Thesis* University of Wisconsin, Madison, WI, USA (available as *Wisconsin Medical Physics Report* No WMP-102)
Motz J W and Dick C E 1975 *Med. Phys.* **2** 259–70
Nemet A, Cox W F and Hills T H 1953 *Br. J. Radiol.* **26** 185–92
Reiss K H 1959 *Z. Angew. Phys.* **11** 184–8
Reiss K H and Steinle B 1973 *Tabellen zur Röntgendiagnostik II* (available from Siemens AG, UBMed, Erlangen, Fed. Rep. of Germany)
Shreider Y A 1966 *The Monte Carlo Method* (Oxford: Pergamon Press)
Spiegler G 1957 *Physikalische Grundlagen der Röntgendiagnostik* (Stuttgart: Thieme Verlag) ch. 5
Stargardt A and Angerstein W 1975 *Fortschr. Geb. Roentgenstr.* **123** 364–9
Storm E and Israel H 1970 *Nuclear Data Tables* **A7** 565–681
Trout D, Kelly J P and Larson V L 1975 *Am. J. Roentgenol.* **124** 404–11
Wilsey R B 1921 *Am. J. Roentgenol.* **8** 328–38
Zieler E 1966 *Bildgüte in der Radiologie* ed F E Stieve (Stuttgart: Fischer Verlag) pp 33–44